# Analyst

Accepted Manuscript






ROYAL SOCIETY OF CHEMISTRY

www.rsc.org/analyst

# Macroscopic Fourier Transformed Infrared scanning in reflection mode (MA-rFTIR), chemical imaging of cultural heritage artefacts in the mid-infrared range

Stijn Legrand [a], Matthias Alfeld [a, b], Frederik Vanmeert [a], Wout De Nolf [a] and Koen Janssens [a],

[a] University of Antwerp, Department of Chemistry, Groenenborgerlaan 171, B-2020 Antwerp, Belgium

[b] Deutsches Electronen Synchrotron (DESY), P06 Beamline, PETRA-III, Notkestrasse 85, D-22607, Hamburg, Germany



## Abstract

In this paper we demonstrate that by means of scanning reflection FTIR spectroscopy, it is possible to record highly specific distribution maps of organic and inorganic compounds from flat, macroscopic objects with cultural heritage value in a non-invasive manner. Our previous work involved the recording of macroscopic distributions of chemical elements or crystal phases from painted works of art based on respectively macroscopic X-ray fluorescence or X-ray diffraction analysis. The use of infrared radiation instead of X-rays has the advantage that more specific information about the nature and distribution of the chemical compounds present can be gathered. This higher imaging specificity represents a clear advantage for the characterization of paintings and artists materials. It allows the distribution of metallo-organic compounds to be visualized and permits to distinguish between pigmented materials containing the same key metal.

The prototype instrument allows to record hyperspectral datacubes by scanning the surface of the artefact in a contactless and sequential single-point measuring mode, while recording the spectrum of reflected infrared radiation. After the acquisition, spectra, line intensities of individual bands and chemical distribution maps can be extracted from the datacube to identify the compounds present and/or to highlight their spatial distribution. Not only is information gained on the surface of the investigated artefacts; also images of overpainted paint layers and if present, the underdrawing, may be revealed in this manner. A current major limitation is the long scanning times required to record these maps.

# 1 Introduction

In the study of historical paintings and more specifically as a preparation for restoration activities of such artefacts, it usually is of great relevance to investigate which pigments are present and how these are distributed at or below the painting surface. A large number of analytical techniques have been developed that can be used for the identification of artists' materials. However, many of these techniques require destructive sampling or some form of sample preparation. Therefore, such analyses are restricted to point measurements while the number of investigated locations is usually limited to a minimum. Moreover, in many cases, most of the analysed positions are chosen in the background areas or at the edges of the painting and not in the important pictorial regions in order to minimise any damage to the cultural heritage (CH) artefact being examined.

During the last decades the continued development of non-destructive analytical techniques resulted in instruments with a higher performance and in the miniaturization of such devices. When bench top equipment is employed for works of art, the objects or samples to be analysed need to be moved to a (science or conservation) laboratory. Due to all the necessary precautions regarding e.g. transport, safety, climate control and insurance, this kind of transportation for objects of cultural heritage usually is a fairly costly and difficult undertaking. In case of artefacts that are not possible or very difficult to move, the increased mobility of analytical instruments has made it possible to analyse such objects *in situ*.[1,2,3,4,5,6,7] Since this *modus operandi* barely requires manipulating the object to be analysed, conservators are more willing to give scientists access to works of art for *in situ* measurements.

Some of these non-destructive *in-situ* methods, including X-ray fluorescence (XRF), X-ray diffraction (XRD), fibre optics reflectance spectroscopy (FORS) and Raman spectroscopy commonly are only used for spot analyses and, on average, require several minutes to record a spectrum from a single sample position. After the point analysis campaign, and on the basis of visual information and extra data such as knowledge about the artist's painting technique, the obtained results may be extrapolated to the entire painting. However, making such extrapolations is error prone. Thus, hyperspectral analysis methods, where a spectral response is obtained from all points of the examined surface rather than from a limited number of (hopefully) representative spots are preferred; such methods have only become recently available. An example of this class of analytical methods is Macroscopic X-Ray Fluorescence (MA-XRF).[8] While it is possible to perform *in situ* imaging at decimetre to metre length scales by means of this method, the elemental distribution maps acquired lack the possibility to differentiate between pigments that consist of similar key elements

(to see, e.g., the difference between hematite, goethite and limonite) and to detect low z-elements that are characteristic of many organic pigments and dyes.

Infrared-based analytical methods use radiation of energy comparable to that of the vibrational levels present in molecules. Therefore, these techniques are better suited than others for differentiating between (similar) chemical compounds. In addition, infrared measurements in reflection mode allow to perform analyses in a non-contact and a non-destructive manner.

With the development of infrared reflectography,[9] instrumental imaging of cultural heritage materials in the infrared region of the electromagnetic spectrum became possible. An IR-transparent lens can be used to capture radiation reflected by the object under study and refocus it on an IR-sensitive camera. Initially vidicon imaging systems, sensitive for infrared light, were used for this purpose. Nowadays these are mostly replaced by focal plane arrays (FPA), sensitive in the same or adjacent spectral regions; these devices allow to directly record IR-intensity images.

At first, only one or a few spectral bands could be used for imaging. Their spectral region was optimized in order to minimize the absorption of IR light by the overlying paint layers and thus to enhance the contrast between the underdrawing and the overlying painting. To obtain more than one spectral band with the same FPA, filters can be placed in front of the FPA. While the first generations made use of manually placed filters, liquid tuneable filters[10] were employed in later generations. In case that only a few to a few tens of spectral bands are used, the term multispectral imaging is employed. The use of large spectral bands results in a good signal-to-noise contrast ratio in the obtained images, but yields only a limited spectral resolution. Thus, identification of the chemical compounds present, based solely on the recorded image data, is not possible. However, it may still be possible to differentiate between e.g., two adjacent pigment areas when their reflectance characteristics in the IR region are different.

*NIR imaging.*

Detectors for imaging in the NIR range of radiation may comprise arrays of thousands by thousands of individual detector elements. These detectors are often modified charged coupled devices (CCD)[10], photo detectors or thermal detectors. Since it is more difficult to create detector arrays, sensitive towards the longer wavelengths of IR-light, with comparable lateral resolution and spectral response as those available for visible light, the FPAs used in IR camera systems mostly comprise only tens up to maximum a few hundreds of pixels in each dimension. In order to analyse macroscopic objects such as paintings with a sufficiently high lateral resolution, mosaic assemblies of smaller images are then recorded.

The use of lenses in combination with flat detectors such as FPAs introduces distortions in the resulting images. To avoid such problems, an alternative approach[11,12] was developed, based on point-by-point rather than full-field scanning (or whisk-broom approach) of the object. This solution involves the use of fibre-optics for guiding the reflected IR radiation to the detectors. The moving head of the scanner contains only the main optical system, responsible for emitting the primary radiation and capturing the reflected radiation. The reflected radiation is focussed at the entrance of the optical fibres and guided towards the detectors present in the stationary part of the scanner. This approach makes the scanning setup lighter, enables the use of higher scanning speeds and avoids that vibrations are passed along from the moving scanner to the detectors.

Every optical fibre directs radiation to a different interference filter/detector combination. In this instrument, three Silicon (Si) and 12 Indium Gallium Arsenide (InGaAs) detectors are used for near infrared (NIR)-imaging. Resulting in a fast scanning capability with a maximum rate of 2 kHz at a 250 µm step size, covering almost the whole NIR-band (800-2300 nm or 12 500–4350 $cm^{-1}$). However, since this spectral range is only divided into a limited number of bands, data sets with only a limited spectral resolution are obtained.

Recent instrumental evolution has resulted in imaging systems that can record data over an increased number of spectral bands; to differentiate these systems from the older multispectral systems they are called *hyper*spectral imaging systems. No exact boundary between the two imaging systems can be found in literature, but a general convention states that multispectral systems possess a number of bands that is distinctly lower than the number of steps used in the spatial dimension. At the other hand, in hyperspectral systems, the number of bands is of the same order as the number of spatial steps.[13,14]

Improvements in the spectral resolution of multi- or hyperspectral NIR imaging systems can be realised via the use of a dispersive element such as a grating.[15] The grating disperses the radiation depending on its wavelength and the intensity of the dispersed bundle of radiation is recorded by different rows of the array. The number of spectral bands in these systems is therefore determined by the number of elements in the FPA. The second dimension of the detector can still be used for the spatial domain and thus allows the acquisition of line scans, allowing faster scanning speed.

*MIR imaging.*

The previous cited imaging devices are all active in the near infrared (NIR) region, where overtone and combination bands of the functional groups of chemical compounds are present. This spectral region allows to differentiate to a certain degree between the compounds present in analysed objects, but lacks the specificity that can be obtained from mid infrared (MIR) spectral data. Until

recently,[16] it was not possible to perform macroscopic non-destructive MIR imaging on macroscopic artefacts such as paintings. Rosi et al. recently employed a hyperspectral imaging system to record distribution images over a limited region of the MIR-range (900-1440 $cm^{-1}$) with a spectral resolution of 4 $cm^{-1}$. The system employed combines a 256 x 256 pixel FPA detector coupled to an interferometer, allowing to record in one measurement a complete hyperspectral data cube. The investigation of an area of 9 x 9 $cm^2$ required a collection time of 80 s.

In what follows, we describe a mobile point-by-point NIR-MIR (7500-375 $cm^{-1}$) reflection mode scanning device for non-invasive and non-destructive hyperspectral imaging of macroscopic two dimensional objects such as paintings. Contrary to previously described systems, this scanning setup does not employ a (costly) FPA, but a single point detector incorporated in a compact and inexpensive FTIR spectrometer. Thus, FTIR data over the full spectral range are recorded at each position. The entire infrared spectrometer is part of the moving scanning head. This avoids the use of chalcogenide fibre optics that have a spectral cut-off at ca. 900 $cm^{-1}$.

# 2 Experimental

2.1 *MA-rFTIR setup*.

Local irradiation of the examined artifacts and spectrum acquisition were performed by means of a Bruker Alpha FTIR spectrometer, equipped with a frontal reflection module (20°/20° geometry) and a coaxial visual camera. The spectrometer incorporates a globar IR-source and a deuterated triglycine sulphate (DTGS) detector. Such a detector has a slower response time and is less sensitive than a mercury cadmium telluride (MCT) detector, but it has the advantage of operating at room temperature, making it more useful for *in-situ* measurements. In addition, DTGS-detectors have an increased spectral response towards the far infrared (FIR) region than most MCT-detectors.

Spectra acquisition and storage is done with the Bruker OPUS 6.0 software package. The instrument is calibrated using a polystyrene film at room temperature on a weekly basis. Before every scan, the background is recorded during 15 minutes by placing a gold coated mirror in front of the reflection module. This background spectrum is then used to correct each spectrum for atmospheric absorptions during the scan.

During most scans, the infrared spectra are recorded during an interval of *ca.* 10 seconds per point, where an individual spectrum is saved roughly every second, having a spectral resolution of 4 $cm^{-1}$. When consecutive spectra in one point differ too much, the spectrometer's control software automatically rejects the last spectrum, resulting in a lower number of spectra in such locations. This is often the case when the analysed surface is not smooth.

Since the actual measuring time is the most time consuming component in the total scan time, it is important to keep it as short as possible. The abovementioned spectrum acquisition time of *ca.* 10 s per point corresponds to a compromise between spectral quality and scanning speed. Longer measurement times per point result in an improved spectral quality, but the latter usually only results in a marginal improvement of the final image quality. In addition to the time devoted to spectrum acquisition, per recorded position, an additional 6 to 20 s are required for spectrum saving, and for moving to the next point. Thus, it generally does not make sense to use acquisition times per pixel that are shorter than *ca.* 10 s with this system. When a better spectral quality is required than what can be recorded during such an interval, spectra of adjacent or similar points can be combined *a posteriori*.


Figure 1: Photographs of the MA-FTIR scanning setup: a) side- and b) front view.

In this scanning setup (Fig. 1), the FTIR spectrometer is mounted on a motorized scanning stage (Newport Corporation, Irvine, CA, USA). During the scan operation, the spectrometer is moved in the X (maximum travel range: 100 mm) and Y (250 mm range) directions by motorized stages, while the Z (100 mm range) stage allows to position the focal point of the scanner at the surface of the painting prior to the XY movement. This z-position is determined at the centre of the area to be analysed, as the distance where the reflected radiation is detected at the maximum intensity. The entire scanning operation, including stage movement and spectrometer triggering, is controlled by in-house written software. The processing of the individual spectra and the hyperspectral data treatment is performed with self-written routines using the data analysis software package IDL 8.2. The measured reflectance intensity (R) is a combination of both specular and diffuse reflectance components because the infrared radiation impinges on and reflects back from the surface under an angle of 20 degrees.

Because both components contribute to the spectra, neither the Kramers-Krönig nor the Kubelka-Munk transformations can be applied to the spectra. Instead, the reflectance spectra are converted to pseudo-absorbance (A') form using the relation $A' = \log(1/R)$. Unless otherwise noted, all data in this paper are in pseudo-absorbance form.

The beam size at the spectrometers focal point was determined by performing a line scan measurement across a sharp edge between two sample areas made up of calcite ($CaCO_3$) and Prussian blue ($Fe_4[Fe(CN)_6]_4$). After the scan, an error function was fitted to the sigmoidal shape obtained by plotting the band intensity of the cyanide group (1900-2120 $cm^{-1}$) against the lateral coordinate. The full width at half maximum of this function was taken as a measure of the effective size of the IR-beam in the scan direction: values of 1.80 mm (horizontal) x 2.10 mm (vertical) were obtained. The increased beam size in the vertical plane results from the reflection geometry since the IR beam impinges on the analysed surface at an angle. Even though these dimensions were found, smaller details could be visualised, this probably due to the fact that the beams intensity is not equally distributed over the irradiated spot. As a result, smaller step sizes than the beams dimensions are being used in the imaging experiments.

In Table 1, an overview of the scan parameters employed to investigate the 3 paintings described below is provided. The two first paintings were scanned using a slower motor speed, resulting in longer dwell times.

Table 1. Scan parameters employed during MA-FTIR examinations of three paintings

| **Painting** | **Step size (H x V) ($mm^2$)** | **Area examined ($cm^2$)** | **Dwell time/pixel (s)** | **Spectral range ($cm^{-1}$)** |
|---|---|---|---|---|
| Replica | 1 x 1 | 5.5 x 8.0 | 29 | 375 - 4000 |
| Antillean painting | 1 x 1 | 7.6 x 7.6 | 29 | 375 - 4000 |
| Russian Icon | 1 x 1 | 10.2 x 17.2 | 18 | 375 - 7500 |

2.2. *Processing of FTIR hyperspectral data*

After each scan, the series of reflectance infrared spectra are arranged into a three dimensional data cube and converted to pseudo-absorbance values.

Next to the local chemical composition, the recorded reflectance intensity is a function of the local physical parameters of the irradiated area such as grain size and surface roughness. These last two parameters primarily result in an intensity modulation of the total reflection FTIR spectrum, and less

in a change of the spectral features that are recorded. To maximise the chemical contrast in the distribution images, the integrated intensity of the peaks in the pseudo-absorbance spectra is calculated followed by the subtraction of the background relative to a baseline running through the integration limits. As a result, also negative intensities can be obtained. This is typically for bands inverted by the reststrahlen-effect, usually observed for antisymmetric stretching of silicate, sulphate and carbonate pigments. When these bands are used for imaging, the distribution image will be reversed so that the most intense pixels correspond with the most negative intensity. A typical feature of reflectance infrared spectra is that they may show derivative shaped features when the absorption index of the irradiated material is small (see Fig. 3a-c). The centre of these features is situated near the wavenumber where the maximum of the corresponding band would be in a transmission FTIR spectrum. When referring to these bands, the centre wavenumber is used, but the integration limits used for creating the chemical distribution images are shifted towards higher wavenumbers with respect to those appropriate for transmission FTIR imaging. By subtracting the A' baseline value, the reflectance intensity modulation due to surface artefacts is largely eliminated. This procedure is performed on all pixels, resulting in two dimensional distributions of the baseline-subtracted pseudo absorbance values, one map for each spectral feature of interest, reflect the distribution of (a class of) chemical compound(s) in the area examined.

To identify the compounds present, spectra from similar points can be combined into one averaged spectrum of high signal-to-noise ratio. Since published spectra in literature usually are (converted into) transmission spectra, the averaged pseudo absorption spectra are mostly compared with transmission databases[17,18] even though they do not show exactly the same features. Only a few papers identify and assign a collection of pigments in pseudo-absorbance mode without any additional data manipulation.[19,20]

2.3 *Comparative measurements.*

Some of the artefacts discussed below were also examined using other macroscopic scanning methods in order to compare characteristics such as the lateral resolution and the chemical specificity of the resulting distributions. To record MA-XRF images, a self-built scanner was used[8], comprised of a Mo anode X-ray tube, running at 50 kV and 1.0 mA, equipped with a dedicated polycapillary lens, as primary radiation source and four Vortex EX detectors, mounted under different angles relative to the primary excitation beam, to detect the XRF signals emitted by the analysed painting. The resulting XRF-spectra were analysed with PYMCA[21] and converted to elemental distribution maps, using in house written software.

Macroscopic X-Ray Diffraction scanning (MA-XRD) measurements were performed during experiment EC-764 at ID15B beamline of the European Synchrotron Facility (ESRF) in Grenoble, France. A high energy 87.08 keV, 300 x 300 µm primary beam was used during an exposure time of 0.5 seconds per point. Step sizes of 0.8 mm and 0.4 mm were employed. The obtained series of 2D XRD-patterns were analysed and converted to species-specific maps using the XRDUA software package.[22]

2.4 *Examined artefacts.*

To determine the capabilities and limitations of the MA-rFTIR scanner, a series of painted artefacts of various nature was investigated. The first artefact consisted of a replica (8 x 5 cm) of a vegetal pattern present in a decorative border of a 15$^{th}$ century breviary;[23] the replica was prepared using modern and well-documented oil paint materials (see Fig. 2a). Chemical distribution maps were recorded by means of the MA-rFTIR and MA-XRD systems. A second artefact, a relatively simple 20$^{th}$ century panel painting (8 x 8 cm in size, see Fig. 4a), was analysed by means of MA-rFTIR and MA-XRF, allowing for a comparison between the chemical and elemental distribution maps resulting from both methods. The third artefact was a painting with more complex paint stratigraphy, *i.e.*, a 19$^{th}$ century icon (14 x 18 cm in size, see Fig. 6a). The MA-rFTIR distributions recorded from this painting were compared with those obtained by IRR, MA-XRF and MA-XRD.

# 3 Results and discussion

## 3.1 Analysis of a replica painting

In the painted replica shown in Fig. 2, three different iron-based pigments were employed: hematite ($Fe_2O_3$, dark red), goethite (α-FeOOH, ochre) and Prussian blue ($Fe_4[Fe(CN)_6]_4$, dark blue). Besides these iron containing pigments, zinc white (ZnO) was used for the preparation layer, vermillion (HgS) for the brighter red in the fruits and viridian green ($Cr_2O_3 \cdot 2H_2O$) in the green foliage.

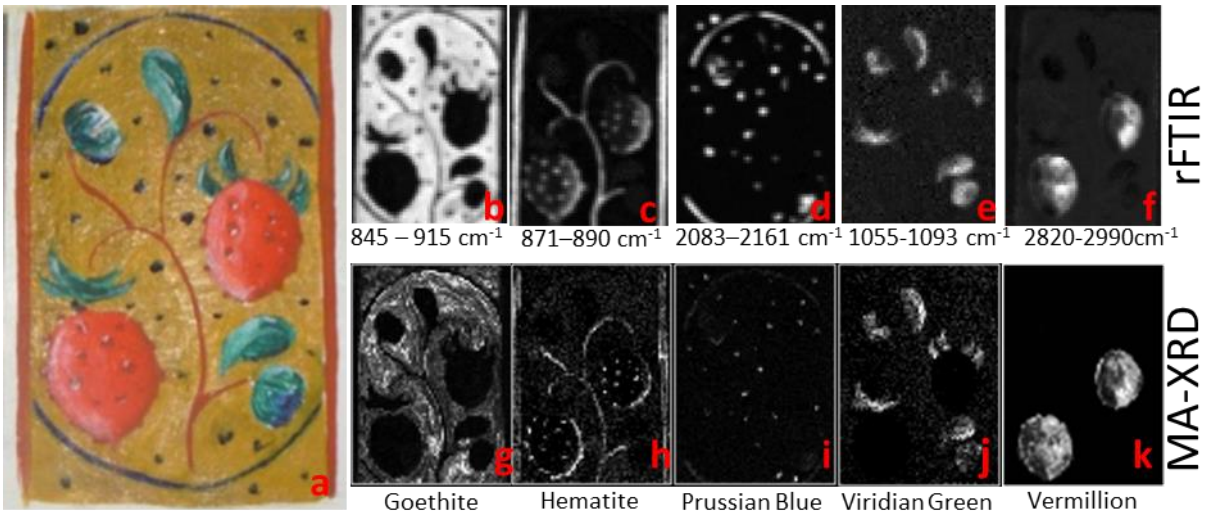


Figure 2: a) Visual image of the replica; upper row: MA-rFTIR chemical distribution images of b) goethite (845-915 $cm^{-1}$), c) Calcite (871-890 $cm^{-1}$), d) Prussian blue (2083-2161 $cm^{-1}$), e) Viridian green (1055-1093 $cm^{-1}$), f) Organic binder (2820-2990); lower row: MA-XRD results of g) goethite, h) hematite, i) Prussian blue, j) Viridian green, k) Vermillion. Lighter tones indicate higher levels of net pseudo absorbance or diffraction intensity.

In Fig. 2, a photograph of the replica and a number of FTIR images (upper row) are shown. Per FTIR image, the wavenumber region used for the net intensity integration is indicated. For comparison, a number of distribution images obtained by MA-XRD (lower row) are included as well. Fig. 3 shows the spectra corresponding to the high intensity areas in the MA-rFTIR distribution maps. To obtain these spectra, an average of 16 spectra, belonging to pixels in the high intensity parts of the corresponding areas, was calculated.

A feature that allows to differentiate goethite from hematite is due to the presence of an –OH group in goethite. This bond results in intense bands (γ-OH: 795 and δ-OH: 892 $cm^{-1}$, marked by "*" in Fig. 3a) that are observed with the mineral goethite. The inverted δ-OH band of goethite ("GO" in Fig. 3) is used for visualising the goethite distribution. Since this is an inverted band, the resulting intensities were inverted in order to correlate the brightest pixels with the most intense (inverted) bands. This resulting distribution (Fig. 2b) shows a strong correlation with the ochre background colour and,

albeit only in the qualitative sense, with the MA-XRD distribution of goethite shown in Fig. 2g. (The difference between Figs. 2b and 2g reflects the sampling depth of both methods.) This spectral region is an example of the instrument's ability to discern between products with (partial) overlapping bands. As visible in Fig. 3a, the δ-OH bending band of goethite ("GO" in Fig 3a) overlaps with the $\nu_2$-$CO_3^{2-}$ bending mode of calcite ("CA" in Fig 3b), however this does not result in interfering distribution maps between these compounds (Figs. 2b and 2c).

It should be noted that the oxide-related bands of hematite (nominally at 458 and 545 $cm^{-1}$) and of goethite (at 458 and 566 $cm^{-1}$) are situated close to each other. Furthermore, the exact position of the bands is prone to shifts in wavenumber due to the pigment's grain size and shape.[24] This explains why the exact wavenumber of these oxide bands is cited in literature to be in a range a few tens of wavenumbers wide. Due to the partial mutual overlap between the two minerals, these bands are not well suited for the chemical imaging in this painting. Moreover, some of the Cr-O bending bands of viridian green (marked by "¤" in fig. 3d), of which the distribution is shown in Figs. 2e and 2j overlap with those of hematite and goethite. The viridian green distribution (Fig. 2e) was obtained by using the Cr=O stretching band ("VG") and shows a good correlation with the corresponding MA-XRD distribution in Fig. 2j.

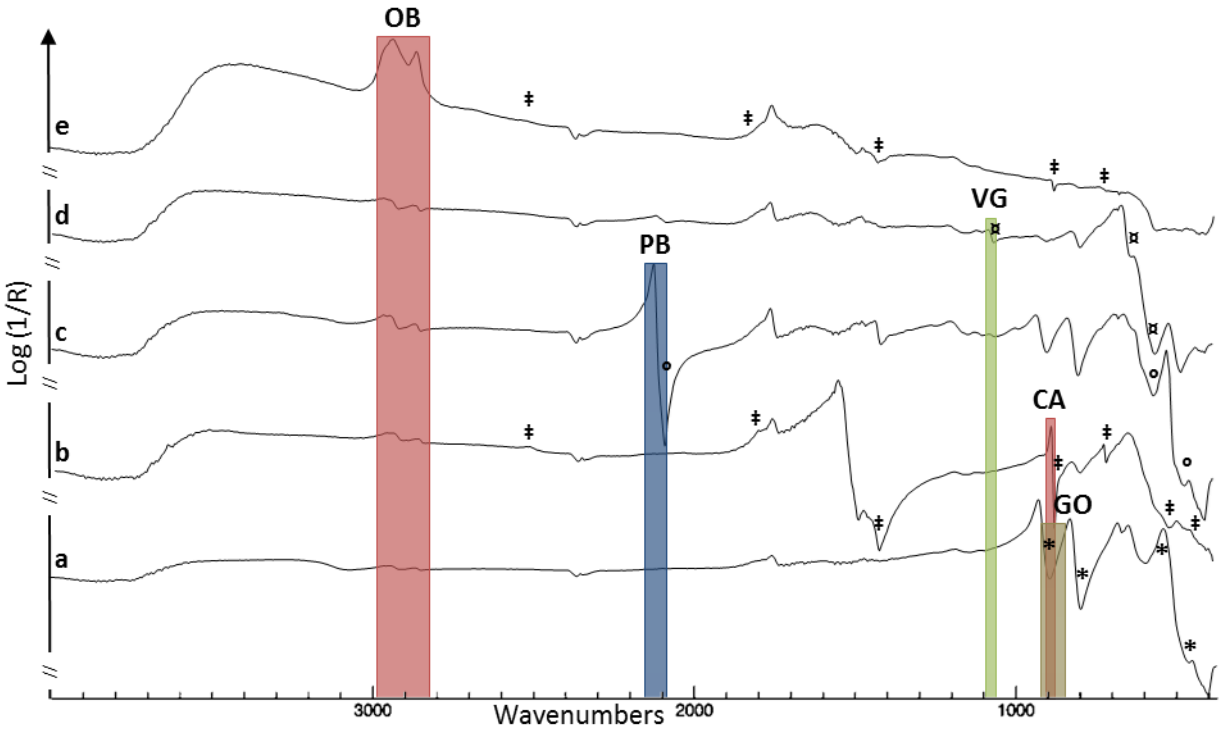


Figure 3: averaged spectra of highlighted zones in Fig. 2; a) goethite, b) calcite/hematite, c) Prussian blue, d) viridian green and e) vermillion

Another way of distinguishing the pigment hematite from goethite in this particular case, is to make use of the fact that only hematite has been mixed with calcite ($CaCO_3$), resulting in strong carbonate signals at 713, 875, 1430 $cm^{-1}$ and the combination bands[19] $v_1 + v_4$ at 1795 $cm^{-1}$ and $v_1 + v_3$ at 2518 $cm^{-1}$, marked by "‡" in Fig. 3b. Accordingly, in the distribution of Fig. 2c, to which calcite contributes, the same highlights as visible in the MA-XRD distribution of hematite (Fig. 2h) can be observed.

Prussian blue is chemically and structurally very different from the previous two iron containing pigments, resulting in an IR spectrum that is fairly specific and is characterized by ν(CN) at 2097, ν(FeC) at 605 and δ(FeCN) bands at 494 $cm^{-1}$ (see "°" in Fig. 3c.) The most intense band, as can be seen in Fig. 3c near 2100 $cm^{-1}$, corresponding to the cyanide group, can be used for chemical imaging (band "PB" in Fig. 3), as shown in Fig. 2d, since there is no danger of interference with signals of other pigments present. An equivalent distribution as that obtainable with MA-XRD (Fig. 2i) is obtained.

Vermillion itself could not be identified using MA-rFTIR since it has its characteristic bands in the FIR-range due to the heavy atomic mass of mercury, but the presence of this compound appears to have an influence on the shape of the observed MIR spectra in the areas where it is present. As a result, the distribution in Fig. 2f, reflecting the intensity of the C-H stretch vibration corresponding to the organic binder of the pigment (band "OB" in Fig. 3) strongly correlates with the MA-XRD distribution of vermillion in Fig. 2k. In the area with high intensity, some mixture of calcite and hematite is also present. As a result, the major calcite related bands are visible in the averaged "vermillion" spectrum shown in Fig. 3e, marked by "‡".

In general, finer details can be discerned in the MA-XRD images, since a smaller spot size (0.3 x 0.3 $mm^2$) was used in the synchrotron based MA-XRD experiment than with the MA-rFTIR scanner. Nevertheless, from Fig. 2 it can be concluded that a species-specific distribution images of good image quality and in which most of the details of the painted representation are visible, can be recorded with the mobile MA-rFTIR scanner. Note that when comparing the different spectra in Fig. 3, the two OH-bending bands of goethite (795 and 892 $cm^{-1}$), seem to appear in most of the averaged spectra. This is a result of the fact that the spot size of the IR-beam is larger than the examined features; this does not seem to disturb the resulting distribution map overly much, however.

## 3.2. Analysis of an Antillean painting

As second case study, we consider a small (8 x 8 cm) 20th century, unvarnished Antillean panel painting shown in Fig. 4a. It consists of a number of coloured areas of appropriate size to be imaged by the scanner; in addition, its stratigraphy is fairly simple, in most cases consisting of only one paint layer applied on a calcite ground. As a result, the ($\nu_1 + \nu_3$) combination band of calcite (shown in Fig. 5) is visible in all recorded FTIR spectra.

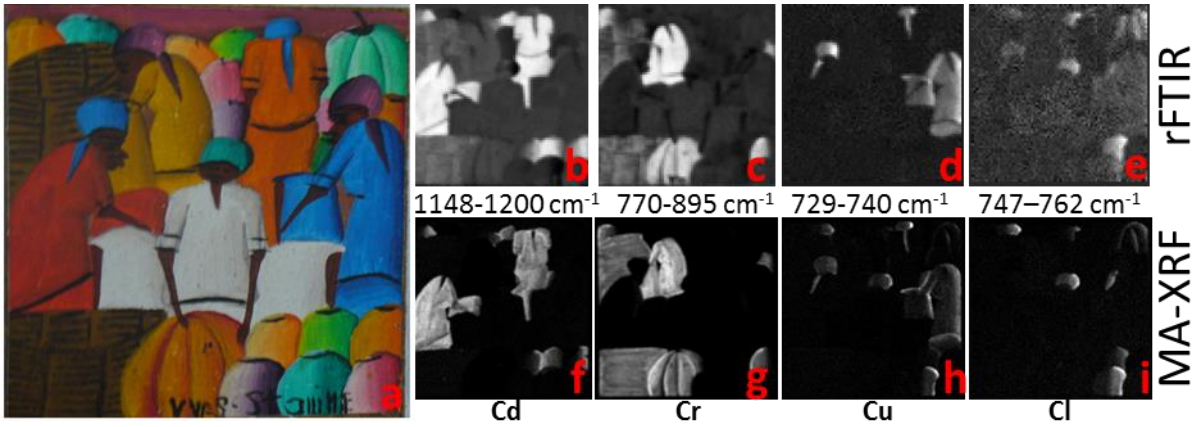


Figure 4: a) Visual image of the Antillean painting; MA-rFTIR chemical distribution images: b) barium sulphate (1148-1200 $cm^{-1}$), c) chrome yellow (770-895 $cm^{-1}$), d) phthalocyanine blue (729-740 $cm^{-1}$) and e) phthalocyanine green (747-762 $cm^{-1}$); elemental distribution maps of f) cadmium, g) chromium, h) copper and i) chlorine. Lighter tones indicate higher levels of net pseudo absorbance or X-ray fluorescence intensity.

Red and orange areas: MA-XRF analysis of this painting (see Fig. 4, lower row) reveals the presence of the elements cadmium, selenium, sulphur and barium (last three distributions are not shown in this article) in the red and orange regions, strongly suggesting that the pigment employed here is cadmium lithopone (CdSe + $BaSO_4$). Cadmium-based pigments have, due to the heavy atomic mass of cadmium, their fundamental bands in the far-IR (FIR) region and therefore cannot be detected with the MIR setup. However, these pigments are often adulterated with the less expensive barium sulphate ($BaSO_4$). The sulphate ions present in this filler are well visible in the MIR-range ($\nu_4$-$SO_4^{2-}$ at 612 and 640 $cm^{-1}$, $\nu_1$-$SO_4^{2-}$ at 983 $cm^{-1}$ and $\nu_3$-$SO_4^{2-}$ at 1079, 1126 and 1202 $cm^{-1}$). [19,25] These vibrational bands confirm the presence of barium sulphate and thus cadmium lithopone in the orange areas. The map in Fig. 4b (1148-1200 $cm^{-1}$) shows the distribution of the sulphate ion via its inverted antisymmetric stretching vibration mode ($\nu_3$-$SO_4^{2-}$) which is strongly correlated to the Cd MA-XRF maps of Fig. 4f. Yellow areas: Based on the MA-XRF-data, the main yellow pigment present in this painting contains the elements lead and chromium and in the FTIR spectra it is identified by its chromate- ($\nu_4$-$CrO_4^{2-}$ at 888 $cm^{-1}$) and sulphate- ($\nu_4$-$SO_4^{2-}$ at 604 and 630 $cm^{-1}$) ion bands as chrome yellow ($PbCr_{1-x}S_xO_4$), a pigment that is in use since the 19th century. The map in Fig. 4c is based on the

$CrO_4^{2-}$ inverted asymmetric stretch (770-895 $cm^{-1}$) and shows a good correlation with the chromium XRF image (Fig. 4g). Even though the fact that both barium sulphate and chrome yellow comprise sulphate groups in their molecules, no hindering interferences between these distributions occurred. The presence of heavier lead instead of barium resulted in a shift towards lower wavenumbers for sulphate bending and stretching bands for the chrome yellow pigment. Besides this shift, the sulphate bands in chrome yellow are of lesser intensity and broadened in comparison to those of barium sulphate. The combination of these effects resulted in interference-free distribution images.

Blue and green areas: The blue and green pigments present in this painting could be identified as phthalocyanine-based pigments. Since this group of pigments was only discovered in the 1930s, their presence confirms the presumed 20th century origin of the painting. The absence of the N-H bending band at 1003 $cm^{-1}$ (Fig. 5g), suggests that the phthalocyanine molecules are present as organo-metalocomplexes. Together with presence the metal-ligand vibration at 898 $cm^{-1}$, typical for copper, these pigments are identified as copper-phthalocyanine. This identification is confirmed by the of copper distribution image, obtained by MA-XRF (see Fig. 4h).

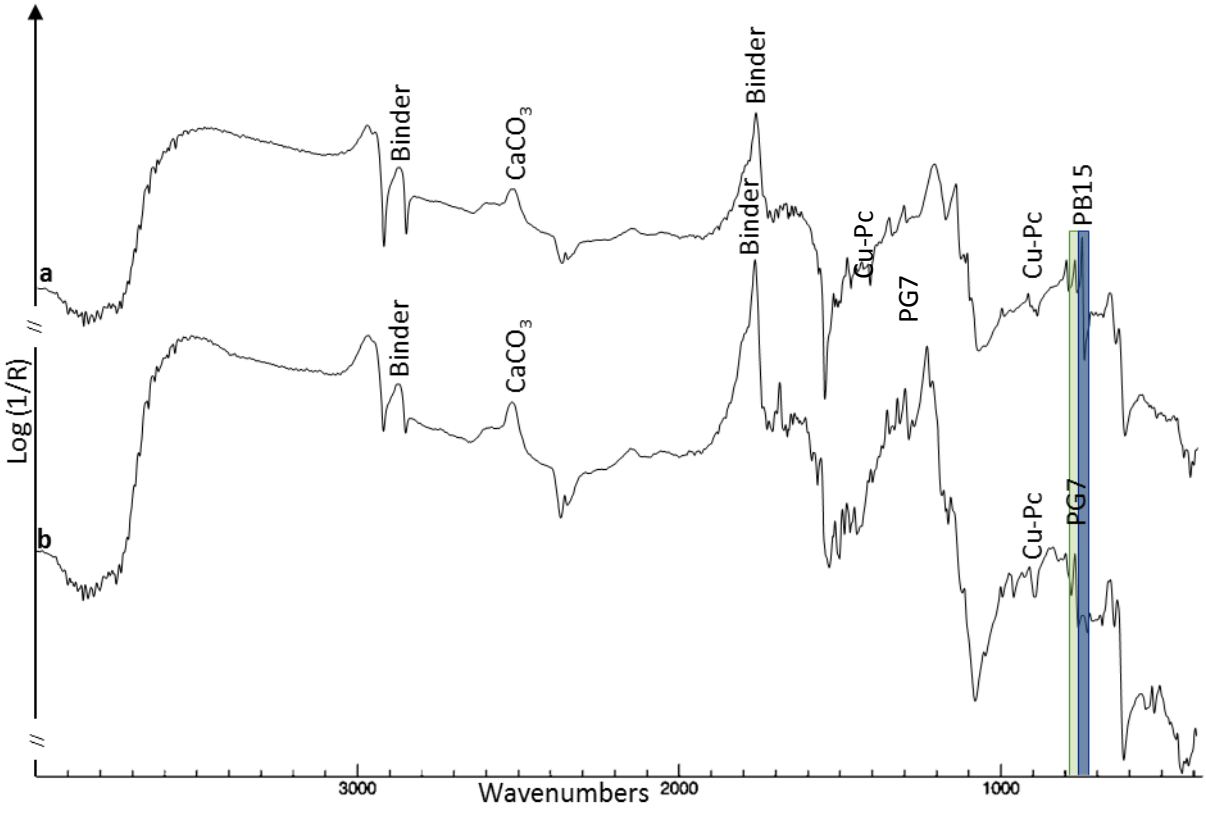


Figure 5: Pseudo-absorption converted reflectance spectra of the phthalocyanine pigments a) PB15 and b) PG7; "Cu-Pc" marks the band assigned to the copper-phthalocyanine vibration; "PB15" marks the band used for imaging the blue pigment, while "PG7" marks the band used for the green pigment; "$CaCO_3$" marks the most intense calcite band and "Binder" those due to the binding medium.

The phthalocyanine-blue (PB15) distribution (Fig. 4d) can be visualized by means of its C-H out-of-plane bending mode at 729-740 $cm^{-1}$ (see Fig. 5a). Phthalocyanine green (PG7) is a partially chlorinated version of PB15. This substitution results in a shift of the C-H out-of-plane bending mode band towards higher wavenumbers, in this case to 747-762 $cm^{-1}$ (see "Fig. 5b). Therefore these modes can be used for imaging the distribution of PG7 (Fig. 4e) as well as that of PB15 (Fig. 4d). As a comparison, the copper and chlorine XRF-maps are given in Fig. 4h and Fig. 4i. Since copper is present in both PB15 and PG7, the MA-XRF copper map resembles the sum distribution of both these pigments. It is possible, however, to distinguish between these two pigments in the MA-XRF data by considering the chlorine distribution (Fig. 4i) since the latter element is only present in PG7. The species-specific MA-rFTIR maps, however, allow to visualize the distribution of these two highly similar pigments in a more straightforward and reliable manner.

## 3.2. Analysis of a 19th century Saint Nicholas Icon

As a third case study with a more complex stratigraphy, MA-rFTIR images from a 19th century Russian house icon depicting Saint Nicholas of Myra, painted on a wooden panel (14 x 18 cm) were recorded. This artefact, visible in Fig. 6a, has been subjected to different non-destructive imaging methods.


Figure 6: a) Visual photograph of the Saint Nicholas' icon; the arrow indicates the blue sleeve of the saint; b) corresponding IRR image; c) Total MA-rFTIR reflectance image in the spectral range corresponding to the IRR image; d) underdrawing (MA-rFTIR); e) decorative bands on the stole (MA-rFTIR); f) Zn distribution (MA-XRF); g) assymetric carboxylate stretching mode

of zinc soap (MA-rFTIR); h) Ultramarine (MA-XRD) and i) Ultramarine (MA-rFTIR distribution, Al,Si-O bending mode). Lighter tones indicate higher levels of net pseudo absorbance or diffraction intensity.

The visualization of hidden underdrawings in paintings is traditionally performed via IRR imaging, as illustrated in Fig. 6b. This reflectogram was obtained with a SIRIS camera system,[26] sensitive in the NIR-range (900-1700 nm or 11 111-5882 $cm^{-1}$). Since there is a spectral overlap (1333-1700 nm or 7500-5882 $cm^{-1}$) between the SIRIS camera system and the MA-rFTIR scanner, similar results can be obtained with the latter setup when the recorded FTIR spectra are treated in a similar manner as done by the SIRIS camera software: the reflectance spectra are used in total reflection mode, no baseline subtraction is performed and the total reflectance intensity is summed within a wide spectral range (7500–5882 $cm^{-1}$ in this case). The result is shown in Fig. 6c; comparison with the IRR image of Fig. 6b shows that even at a lower lateral resolution, the MA-rFTIR result shows most of the details present in the IRR. Since a wide spectral band is used for such imaging techniques, more components than solely the underdrawing may contribute to the resulting images. An advantage of the MA-rFTIR scanner is that simultaneously to using the wide NIR range, several narrower spectral ranges in the MIR part of the spectrum can be used for the imaging of specific compounds, and that these spectral ranges do not need to be specified prior to the measurements (as is the case when filters are employed in NIR-imaging setups). Narrowing a spectral range for imaging purposes has the advantage that this allows scientists to separate the different contributions to wideband images. For example, a detailed examination of the light green decorative lines and crosses on the stole of the Saint that are visible in the IRR image shows that these are likely features that were added in the final phase of the painting and do not correspond to any carbon-based drawing made in the initial phases. When considering more narrow spectral bandwidths in the NIR, the chemical distribution image of Fig. 6e (5358-6134 $cm^{-1}$) can be obtained that only shows the details of the stole, while the carbon-based underdrawing (without stole details) is present in another non-overlapping spectral range (4325-4775 $cm^{-1}$, Fig. 6d; note that in order to obtain the maps 6d and 6e, the intensity of the reflection spectra was employed without the usual conversion to pseudo-absorbance form). The NIR-band to which these spectral ranges belong, is known for the presence of combination and overtone bands of the fundamental MIR bands. Recently, these bands have successfully been used for mapping paint binders in Early Renaissance paintings[27]. Even though this paper shows the possible use of those bands, they were not used as such for this experiment. The narrower NIR bands were solely used for their ability to differentiate between the underdrawing and the overpainted detail.

The distribution of Zinc white (ZnO), present in the grey background, the beard of the figure and the decorations of the stole can be obtained via the intense (and perturbed) reflection FTIR band around 500 $cm^{-1}$; in transmission spectra this band is present as a broad spectral feature between 400 and

500 $cm^{-1}$. Because multiple metal-oxide bands belonging to different metals are present close to each other in this spectral region, distribution images with good contrast are difficult to obtain based on the Zn-O stretching mode. A better result can be obtained by using the asymmetric $COO^-$ -stretching mode, as shown in Fig. 6g (1537-1560 $cm^{-1}$). This band is shifted in the spectrum due to the saponification of the binding medium under the influence of zinc ions[28]. When comparing the distribution of the element zinc (Fig. 6f) with the distribution of the zinc soap (Fig. 6g), one can see that the intensity of the zinc soap is lower in the grey background area than what would be expected based on the intensity in the MA-XRF Zn distribution image. This may be due to the fact that the zinc oxide in the stole decoration is not present in the form of pure zinc white, but as cobalt green ($CoO{\cdot}ZnO$) mixed with chromium oxide ($Cr_2O_3$). This is consistent with the correlated presence of zinc, cobalt and chrome in the blue-green decorative stripes and crosses of the stole as revealed by MA-XRF (resulting Co and Cr elemental distributions are not shown in Fig. 6). The data suggests that the different chemical environments of the zinc ions in the blue-green and grey areas of the painting have resulted in a different spectral response and possibly in different degrees of saponification of the binding medium.

One of the limitations of MA-XRF is that it is insensitive to low-Z elements. These elements have low energetic XRF-signals that are absorbed by the ambient air; consequently, generally it is not possible to visualize any elements lighter than potassium. This absorption can be avoided by working under vacuum or (more realistically) by replacing the ambient air by a helium flow; however, the latter method may induce stress into the painting, which can result in damage. Because of their lower atomic mass, chemical bonds between low Z-elements and oxygen have their fundamental bands in the MIR range of the electromagnetic spectrum, making MA-rFTIR a possible complementary technique to MA-XRF. The pigment ultramarine ($Na_{8-10}Al_6Si_6O_{24}S_{2-4}$) is well suited to demonstrate this complementarity since this inorganic pigment consists only of low Z-elements and thus is hard to detect by means of MA-XRF. Fig. 6i demonstrates that by using the pseudo absorbance in the 465-525 $cm^{-1}$ range (Al, Si-O bending mode[29]), MA-rFTIR allows to create a clear map (Fig. 6i) of the distribution of this pigment. The presence of artificial ultramarine is consistent with the 19$^{th}$ century origin of the icon. This pigment is chemically identical to the expensive medieval ultramarine pigment which was obtained from the semi-precious stone lapis lazuli, at that time exclusively mined in the Afghan mountains. In Fig. 6i and Fig. 6h, the ultramarine distributions obtained by MA-rFTIR and MA-XRD are compared. Both distributions show that only the blue part of the gospel book was painted with this pigment; the Saint's sleeve (see arrow in fig. 6) even though being painted in a similar blue, is not highlighted in these distributions, since it was rendered using Prussian blue.

# 4. Conclusion

By means of the prototype MA-rFTIR scanner that is described in this paper, we demonstrate that the scanning reflectance Fourier transformed mid infrared technique is useful is for *in situ* non-destructive chemical imaging of planar cultural heritage artifacts. Since this device scans the object point-by-point, while recording full spectra over an extended MIR-range (7500-375 $cm^{-1}$) at each position, it is possible to identify the compounds present and visualize their distribution based on their MIR fingerprint features.

When compared to MA-XRF elemental distributions, the obtained chemical distributions show a good correlation with the elemental maps when the chemical element in question is only present in one pigment. MA-rFTIR can deliver complementary information for pigments that cannot be detected or identified in a unique manner by means of MA-XRF. When differentiating between multiple pigments that contain the same characteristic elements, the chemical distribution maps obtained by MA-rFTIR show good agreement with those obtained by MA-XRD.

By analysing different works of art of increasing complexity in terms of paint stratigraphy and pigment variety, the possibilities and some of the drawbacks of MA-rFTIR could be inventoried:

the investigation of a replica of a vegetal decoration was useful to demonstrate the ability of the method to differentiate between various iron-containing pigments. Since these pigments are available in different colours, distinguishing between these pigments can help to understand the artist's techniques and to restore altered paintings back to their original status. The analysis of an Antillean panel painting highlighted the ability of MA-rFTIR to imagine the distribution of different phthalocyanine pigments. This is important since many pigments developed during the last century are organic. Moreover, some organic dyes such as lakes are in use since antiquity and are hard to identify by non-destructive methods. The analysis of a $19^{th}$ century Russian icon allows to demonstrate the capability of the instrument to visualize overpainted underdrawings and to record the distribution of pigments based on light Z-elements such as ultramarine.

Based on these first results, future analysis campaigns on old masterpieces should be undertaken to obtain a better understanding of the chemical imaging of pigments and overpaintings.

A major important limitation of the prototype MA-rFTIR instrument described above, is the time required to record a hyperspectral data set. However, many possibilities are available to improve this aspect, including the use of a more powerful source of MIR radiation and of larger beam focusing and/or collection optics for the reflected radiation.

Another limiting factor in this process is the fact that the majority of historic paintings is covered by a varnish layer to protect and saturate the underlying painting. Such layers absorb most of the MIR

radiation and as a result strongly disturb the results. Fortunately not all paintings are covered by a varnish layer and from many paintings under restoration, the varnish is removed in the preliminary phases of the treatment. Similar to other forms of mobile FTIR, MA-rFTIR could then be used in optimal conditions once or several times during a restoration campaign. Beside these unvarnished paintings, it is also relevant to investigate in greater detail the possibilities and limits of MA-rFTIR investigations of thinly varnished paintings; experience has shown that, in a number of such cases, by means of portable FTIR devices such as the Bruker Alpha, meaningful spectral features can still be recorded.

## Acknowledgements

The author would like to thank Dr. Geert Van Der Snickt for painting the replica of the 15th century breviary and Prof. Joris Dik of TU Delft for many discussions on macroscopic imaging of works of art, Dr. Arie Wallert of the Rijksmuseum Amsterdam is acknowledged for the recording of the infrared reflectography and the X-ray radiography of the 19th century Russian Icon. We acknowledge the European Synchrotron Radiation Facility for provision of synchrotron radiation facilities and we would like to thank Dr. Veijo Honkimäki for assistance in using beamline ID15B.

## References

1 C. Miliani, F. Rosi, B. G. Brunetti, A. Sgamellotti, *Acc. Chem. Res.*, 2010, **43**, 728-738
2 C. Miliani, F. Rosi, I. Borghia, P. Benedetti, B. G. Brunetti, A. Sgamellotti, *Appl. Spectrosc.*, 2007, **61**, 293-299
3 L. De Viguerie, P. Walter, E. Laval, B. Mottin, V. A. Solé, *Angew. Chem. Int. Ed.*, 2010, **49**, 6125-6128
4 A. Romani, C. Clementi, C. Miliani, G. Favaro, *Acc. Chem. Res.*, 2010, **43**, 837-846
5 G. Chiari, *Nature*, 2008, **453**, 159
6 F. Rosi, C. Miliani, C. Clementi, K. Kahrim, F. Presciutti, M. Vagnini, V. Manuali, A,. Daveri, L. Cartechnini, B. G. Brunetti, A, Sgamellotti, *Appl. Phys. A: Mater. Sci. Process.*, 2010, **100**, 613-624
7 F. Rosi, V. Manuali, T. Grygar, P.Bezdicka, B. G. Brunetti, A. Sgamellotti, L. Burgio, C. Seccaroni, C. Miliani, *J. Raman Spectrosc.*, 2011, **42**, 407-414
8 M. Alfeld, K. Janssens, J. Dik, W. de Nolf, G. van der Snickt, *J. Anal. At. Spectrom.*, 2011, **26**, 899-909
9 J. R. J. Van Asperen de Boer, *Applied Optics*, 1968, **7**, 1711-1714
10 J. R. Mansfield, M. Attas, C. Majzels, E., Cloutis, C. Collins, H. H. Mantsch, *Vib. Spectrosc.*, 2002, **28**, 59-66
11 C. Bonifazzi, P. Carcagni, R. Fontana, M. Greco, M. Mastroianni, M. Materazzi, E. Pampaloni, L. Pezzati, D. Bencini, *J. Opt. A: Pure Appl. Opt*, 2008, **10**
12 C. Daffara, E. Pampaloni, L. Pezzati, M. Barucci, R. Fontana, *Acc. Chem. Res.*, 2010, **43**, 847-856
13 C. Fisher, I. Kakoulli, *Reviews in conservation*, 2006, **7**, 3-16
14 H. Liang, *Appl. Phys. A: Mater. Sci. Process.*, 2011 , **106**, 309-323
15 J. K. Delaney, J. G. Ziebel, M. Thoury, R. Litteton, K. M. Morales, M. Palmer, E. Rene de la Rie, *Proc. of SPIE*, 2009, **7391**,
16 F. Rosi, C. Miliani, R. Braun, R. Harig, D. Sali, B. G. Brunetti, A. Sgamellotti, *Angew. Chem. Int. Ed.*, 2013, **52**, 1-5
17 S. Vahur, A. Teearu, I. Leito, *Spectrochimica Acta A: Molecular and Biomolecular Spectroscopy*, 2010, **75**, 1061-1072
18 K. Castro, M, Perez, M. D. Rodrieguez-Laso, J. M. Madariaga, *Anal. Chem.*, 2003, **75**, 214-221
29 C. Miliani, F. Rosi, A. Daveri, B.G. Brunetti, *Appl. Phys. A: Mater. Sci. Process.*, 2012, **106**, 295-307
20 D. Buti, F. Rosi, B. G. Brunetti, C. Miliani, *Anal. Bioanal. Chem.*, 2013, **405**, 2699-2711
21 V. A. Sole, E. Papillon, M. Cotte, Ph. Walter, J. Susini, *Spectrochimica Acta B*, 2007, **62**, 63-68
22 W. De Nolf, K. Janssens, *Interface Anal.*, 2010, **42**, 411-418
23 G. Van Der Snickt, W. De Nolf, B. Vekemans and K. Janssens, *Appl. Phys. A: Mater. Sci. Process.*, 2008, **92**, 59-68.

24 J. L. Rendon, C. J. Serna, *Clay Miner.*, 1981, **16**, 375-381
25 V. Ramaswamy, R. M. Vimalathithan, V. Ponnusamy, *Adv. Mat. Lett.*, 2012, **3**, 29-33
26 D. Saunders, R. Billinge, J. Cupitt, N. Atkinson, H. Liang, *Stud. Conserv.*, 2006, **51**, 277-290
27 K. A. Dooley, S. Lomax, J. G. Zeibel, C. Miliani, P. Ricciardi, A. Hoenigswald, M. Loew, J. K. Delaney, *Analyst*, 2013, **138**, 4838-4848
28 L. Robinet, M. Corbeil, *Studies in Conservation*, 2003, **48**, 23-40
29 C. Miliani, A. Daveri, B. G. Bruinetti, A. Sgamellotti, *Chemical Physics Letters*, 2008, **466**, 148-151

## Graphical Abstract


Macroscopic Fourier Transformed Infrared scanning in reflection mode (MA-rFTIR), a new tool for the chemical imaging of cultural heritage artefacts in the extended mid-infrared range (7500-375 $cm^{-1}$).